Journal of Alloys and Compounds 928 (2022) 167242

Contents lists available at ScienceDirect

Journal of Alloys and Compounds

journal homepage: www.elsevier.com/locate/jalcom

Uniform and fully decorated novel Li-doped α-Fe_2O_3 nanoparticles for high performance supercapacitors

Asiya M. Tamboli[a,1], Mohaseen S. Tamboli[a,1], Surendra K. Shinde[b], Jihui Byeon[b], Nguyen Tam Nguyen Truong[c,1], Changhee Kim[a], Chinho Park[a,*]

[a] Korea Institute of Energy Technology (KENTECH), 200 Hyeokshin-ro, Naju, Jeollanam-do 58330, Republic of Korea
[b] Department of Biological and Environmental Science, College of Life Science and Biotechnology, Dongguk University, 32 Dongguk-ro, Biomedical Campus, Ilsandong-gu, Siksa-dong, 10326 Goyang-si, Gyeonggi-do, Republic of Korea
[c] School of Chemical Engineering, Yeungnam University, 280 Daehak-ro, Gyeongsan 38541, Republic of Korea

ARTICLE INFO

Article history:
Received 26 May 2022
Received in revised form 14 September 2022
Accepted 15 September 2022
Available online 16 September 2022

Keywords:
α-Fe_2O_3
Li doping
Hydrothermal method
Nanoparticles (NPs)
Specific capacity
Hybrid supercapacitors

ABSTRACT

Supercapacitors are considered emerging energy storage sources owing to their long-term cycling stability, high energy/power density, and rapid charge/discharge process. The performance characteristics of supercapacitors can be enhanced by devising electrodes with highly porous nanostructures through subtle hybridization of active materials and the development of current collectors with tailored nanoarchitectures. Herein, we reported the effect of Li doping on the electrochemical application of the pure α-Fe_2O_3 thin films. The preparation of nanoparticles-like nanostructures of the pure α-Fe_2O_3 and different percentages of Li-doped α-Fe_2O_3 thin films by cost effective and facile hydrothermal method for the supercapacitor application. As-synthesized pure α-Fe_2O_3 and Li doped α-Fe_2O_3 thin films were analyzed by the X-ray diffraction (XRD), and X-ray photoelectron (XPS) spectroscopy, scanning electron microscopy, transmission electron microscopy, and supercapacitor properties. The XRD results revealed the formation of the pure phase of the α-Fe_2O_3 with the rhombohedral crystal structure. XPS results confirmed the Li species existence in the 0.5% Li doped α-Fe_2O_3. The electrochemical properties indicate the 3D chain of the nanoparticle-like surface morphology of pure α-Fe_2O_3 and Li-doped α-Fe_2O_3 are more useful electrode materials for electrochemical application. The calculated values of the specific capacity (Cs) indicate the different percentages of doping of Li are affected by the electrochemical properties of the pure α-Fe_2O_3. The Cs of the optimized 0.5% Li-doped α-Fe_2O_3 (79 mAh g^{-1}) electrode was 1.3-fold higher than that of the pure α-Fe_2O_3 electrode (52 mAh g^{-1}) at a constant scan rate with excellent cycling stability upto 3000 cycles. The electrochemical and surface morphological analysis demonstrate that the 0.5% Li-doped α-Fe_2O_3 electrode is more useful than the pure α-Fe_2O_3 and other electrodes for developing high-rate hybrid supercapacitor-based energy storage devices applications.

1. Introduction

In this present era of digitalization, the rapid growth of portable devices, wireless electronics, hybrid electric vehicles, and the aerospace industry have triggered significant developments over the past few years [1,2]. The most important electrochemical energy conversion and storage devices include batteries and supercapacitors, which stand out because of their potential use in various electrical appliances [3–8]. However, batteries have certain limitations such as high production cost, low power density, and limited life span. By contrast, the supercapacitor has huge potential as a backup power source because of its rapid charge–discharge rate, high power density, fast energy delivery, prolonged cycle life, lightweight, excellent reliability, and flexibility, which can fulfill the growing power requirements of energy storage systems [9–11]. However, supercapacitors lag batteries in terms of energy density. Hence, the idea is to fabricate supercapacitors with increased energy density, while retaining all of their other beneficial features. Supercapacitors are categorized into two types based on the underlying energy storage mechanism, namely electric double-layer capacitors (EDLCs) and pseudocapacitors. EDLCs' function based on ion-adsorption

* Corresponding author.
E-mail address: chpark@kentech.ac.kr (C. Park).
[1] These authors contributed equally.

https://doi.org/10.1016/j.jallcom.2022.167242
0925-8388/

mechanisms at the electrolyte–electrode interface, whereas pseudocapacitors function based on fast redox Faradaic reactions [12].

To date, several electrode materials have been synthesized for use in supercapacitors, including transition metal oxides, transition metal sulfides, carbonaceous materials, chalcogenides, polyoxometalates, conducting polymers, metal-organic frameworks, siloxenes, and Mxene [13–20]. Generally, to fabricate pseudocapacitive electrode materials, transition metal oxides (TMOs) such as CuO, Fe_2O_3, TiO_2, RuO_2, MnO_2, In_2O_3, V_2O_5, Co_3O_4, and Mn_2O_3 are used because they undergo reversible Faradaic reactions [21–28]. The energy densities of these TMOs are considerably higher than those of carbonaceous materials [29]. Among these TMOs, Iron oxide (Fe_2O_3) is an emerging electrode material for supercapacitors because of its features such as abundance in nature, lack of toxicity, cost-effectiveness, high stability, good electrochemical activity, suitable voltage window, and high theoretical capacity (3625 F g^{-1}) [30–33]. However, Fe_2O_3 electrodes have low Cs values (120 −300 F g^{-1}), poor intrinsic electrical conductivity (∼10 −14 S cm^{-1}), and short electrochemical durability. Moreover, Fe_2O_3 undergoes volume expansion during electrochemical reactions, which results in a high electron transfer resistance and unwanted pulverization and accumulation [34–38]. Moreover, for researchers, it is imperative to enhance the electrochemical performance of Fe_2O_3 electrodes to increase their capacitance, power density, energy density, and electronic conductivity. Several studies have reported that TMOs with more than one cation exhibit improved electrochemical activity and conductivity, and for this reason, their performance is superior to that of a single-component electrode. Examples of such materials include Mn-doped Co_3O_4, Cu-doped NiO, F-doped Fe_2O_3, Fe-doped SnO_2, and Cr-, Co-, Ni-, and Cu-doped Mn_3O_4 [27,39–42]. Also, nitrogen/sulfur co-doped graphene hybrid supported N-Fe_2O_3 nanoparticles as the electrode material of supercapacitors [43]. Shinde et al. [44] reported the effect of Mn doping on the electrochemical performance of the hybrid CuO/$Cu(OH)_2$ materials. They concluded that a positive effect on the surface morphology of the Mn doping. Finally, they reported the higher specific capacitance values for 3% Mn doping on the CuO/$Cu(OH)_2$ hybrid electrode. Chougale et al. [45] reported the maghemite iron oxide phase using the electrodeposition method for supercapacitor application. They concluded that the maghemite crystal phase showed more electrical properties than the other phase of Fe_2O_3. The reported specific capacitance values of the 524 F g^{-1} at scan rate of 5 mV s^{-1} in Na_2SO_3 electrolyte for the γ-Fe_2O_3 electrode.

Based on these developments, in the present study, we aim to prepare Li-doped α-Fe_2O_3 nanomaterials with various percentages of Li doping suitable for electrochemical applications by following the hydrothermal method. We confirmed the synthesis of pure α-Fe_2O_3 and Li-doped α-Fe_2O_3 nanomaterials by using different analytical techniques to classify their structural, surface morphological, and electrochemical properties. The pure and Li-doped α-Fe_2O_3 electrodes were systematically tested in a three-electrode system within a potential window of − 0.1–0.5 V in the presence of 3 M KOH. The assembled hybrid asymmetric supercapacitors of 0.5% Li-doped α-Fe_2O_3//AC device provided an outstanding energy density of 28.73 Wh kg^{-1}, power density of 7508 W kg^{-1} with a superior specific capacitance of 136 F g^{-1}.

2. Experimental details

2.1. Chemicals

Ferric nitrate ($Fe(NO_3)_3{\cdot}9H_2O$, 99.99%), lithium nitrate ($LiNO_3$, 99.99%), sodium hydroxide (NaOH), polyvinyl alcohol (PVA) and potassium hydroxide (KOH) were procured from Sigma-Aldrich and utilized as-supplied. Nickel foam (450 μm, thickness: 1.6 mm) was procured from ALANTUM, S. Korea.

2.2. Preparation of pure α-Fe_2O_3 and Li doped α-Fe_2O_3 samples

The α-Fe_2O_3 NPs were synthesized by following the hydrothermal approach. To this end, equimolar concentrated solutions of $Fe(NO_3)_3{\cdot}9H_2O$ and NaOH were prepared in MiliQ water, separately. Both solutions were mixed gradually by using a magnetic stirrer. The resulting solution was moved to a stainless-steel jacketed Teflon reactor in which the hydrothermal reaction proceeded at 100 °C for 6 h. Then, the reactor contents were cooled to room temperature, and the resulting solution was centrifuged and washed several times with MiliQ water; finally, it was washed with ethanol and dried at 60 °C in an oven. To synthesize Li-doped α-Fe_2O_3, we substituted ferric nitrate with 0.5%, 1%, 2%, 4%, and 6% $LiNO_3$. Hereinafter, these samples are labeled Pure FO, LFO0.5, LFO01, LFO02, LFO04, and LFO06, respectively.

2.3. Synthesis of α-Fe_2O_3 and Li-doped α-Fe_2O_3 thin films

Ni foam as a substrate and polyvinyl alcohol (PVA) as a binder were used to screen-print thin-films containing the as-prepared α-Fe_2O_3 and Li-doped α-Fe_2O_3 powders. The constant mass of material deposited on Ni foam for pure α-Fe_2O_3 and Li-doped α-Fe_2O_3 (0.5%, 1%, 2%, 4%, and 6%) electrodes is to be 3 mg cm^{-2}, respectively. The prepared α-Fe_2O_3 and Li-doped α-Fe_2O_3 thin films were allowed to dry naturally and then annealed at 100 °C for 6 h.

2.4. Characterization techniques

The structural analysis and phase purity of the samples were analyzed by X-ray diffraction (XRD) on a PANalytical X′Pert PRO equipped with a monochromator and Ni-filtered Cu K_α(λ = 1.5406 Å) source. The morphological features of the synthesized samples were analyzed by Scanning Electron Microscopy (SEM, Hitachi S-4800 JEOL JSM-7100). Microstructure analysis was carried out using Field-Emission Transmission Electron Microscopy (FE-TEM) with a Tecnai G2 microscope. X-ray photoelectron spectroscopy (XPS) analysis was recorded using an ESCALAB-MKII spectrometer. Brunauer-Emmett-Teller (BET) specific surface area measurement were carried out using Autosorb-iQ and Quadrasorb SI instruments (BELSORP; Tokyo, Japan).

2.5. Electrochemical measurements

The Versa STAT 3 instrument with the classical three-electrode system was used to perform electrochemical measurements. This system consists of the reference electrode (Ag/AgCl electrode), a counter electrode (Pt electrode), and pure Fe_2O_3 and the as-prepared Li-doped Fe_2O_3 electrodes as the working electrodes in 3 M KOH aqueous electrolyte. Electrochemical impedance spectroscopy (EIS) was performed with a frequency range of 1 Hz to 100 kHz.

3. Results and discussion

XRD patterns of the pure α-Fe_2O_3, LFO0.5, LFO01, LFO02, LFO04, and LFO06 materials are showcased in Fig. 1a. The diffraction patterns at 24.00, 33.06, 35.70, 40.86, 49.42, 54.04, 62.39, and 64.13° were ascribed to the (012), (104), (110), (113), (024), (116), (214), and (300) planes, respectively. These diffraction peaks and *hkl* planes correspond to the pure α-Fe_2O_3 phase (JCPDS card No.–00–033–0664). The corresponding 2θ values and Miller indices were assigned to the rhombohedral crystal structure of Hematite with lattice parameters of a = 5.03, b = 5.03, and c = 13.74 Å and space group R-3c. Diffraction peaks other than those of α-Fe_2O_3 were not detected, thus indicating the formation of a pure α-Fe_2O_3 phase. Fig. 1b shows the characteristic peak shift of the XRD patterns. According to this Fig. 1b, the two main peaks at 33.24–33.06° and

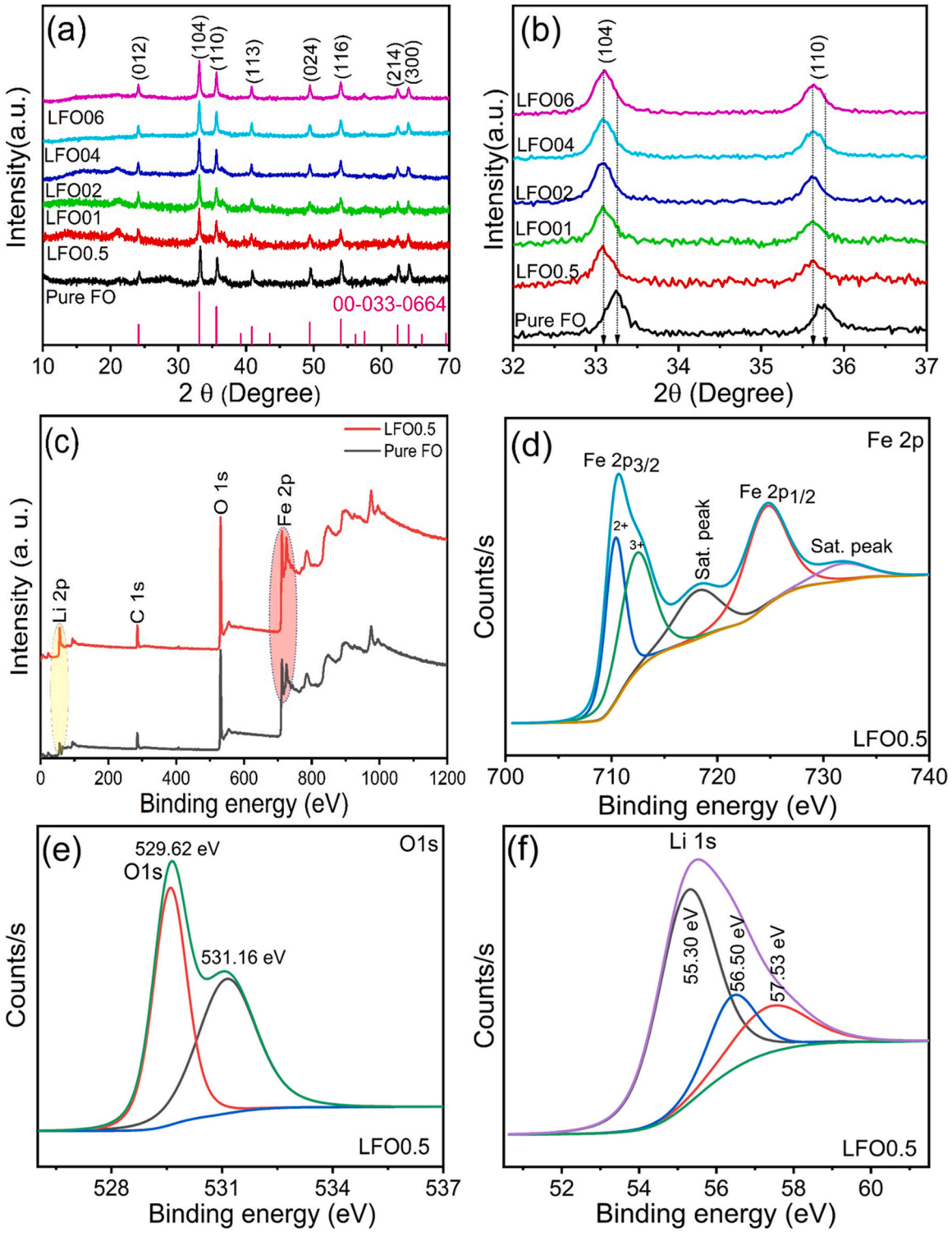

Fig. 1. (a) XRD patterns of the pure α-Fe_2O_3 and Li doped α-Fe_2O_3 at a different percentage of Li, (b) zoomed area of the marked area of the XRD patterns, (c) XPS survey spectra of the pure α-Fe_2O_3 and 0.5% Li doped α-Fe_2O_3 sample, (d-f) core levels of Fe 2p, O 1 s and Li 1 s of optimized 0.5% Li doped α-Fe_2O_3 sample, respectively.

35.70–35.61° are shifted toward a lower angle, indicating changes in the crystal structures owing to the presence of defects in Li and Fe ions. These XRD results indicate the presence of Li ions in the pure α-Fe_2O_3 phase, thus confirming Li ion formation in the Li-doped Fe_2O_3 nanomaterials.

In addition to the observable shift in the crystal lattice parameters, the structural details and compositions of pure α-Fe_2O_3 and the optimized 0.5% Li-doped α-Fe_2O_3 were investigated using XPS analysis. The survey scan spectra of both pure α-Fe_2O_3 and the optimized 0.5% Li-doped α-Fe_2O_3 indicate the presence of Fe and O, and Fe, Li, and O (as shown in Fig. 1c) respectively and confirm the formation of a pure α-Fe_2O_3 phase and Li elements presented in the α-Fe_2O_3 compounds. Fig. 1(d–f) shows the core levels of Fe 2p, O 1 s, and Li 1 s in the optimized 0.5% Li-doped α-Fe_2O_3, respectively. In the Fe 2p spectra of the 0.5% Li-doped α-Fe_2O_3, four main peaks were observed, out of two are related to the main Fe 2p species and the

remaining two correspond to the satellite peaks of the Fe 2p (Fig. 1d). The Fe 2p spectra show the two main characteristic peaks at the binding energies of 710.93 and 724.52 eV, which assigned to the Fe $2p_{3/2}$ and Fe $2p_{1/2}$, respectively. The approximate difference between the main two binding energy peaks of Fe 2p is 13.97 eV, which indicates the presence of Fe^{3+} species in the optimized 0.5% Li-doped α-Fe_2O_3. Additionally, other two peaks at the binding energies of 718.86 and 732.84 eV, which assigned to the satellite peaks of Fe^{2+}, respectively [46,47]. The fitted data of the Fe 2p show one additional peak at the binding energy 713.40 eV, which is due to the Fe^{3+}. These XPS analysis indicates that both species of Fe^{2+} and $Fe^{3+}$are presented in the α-Fe_2O_3 sample. Fig. 1e exhibits the core-level spectra O 1 s, which consists of two main peaks at the binding energies 529.62 and 531.16 eV. The first peak at the binding energy of 529.62 eV, which is related to the lattice oxygen species in the α-Fe_2O_3, and the second peak at the binding energy of 531.16 eV, which is assigned to the chemisorbed oxygen species on the surface, respectively [48]. Similarly, the core level spectra of the Li are shown in Fig. 1f. The Li 1 s spectra indicate the peak at the binding energy of 55.30 eV, which is related to the Li-O bond [49]. The observed Li-O bonds indicate Li specie is existing in 0.5% Li doped α-Fe_2O_3 [50]. XPS results confirmed the doping of the Li specie in the pure α-Fe_2O_3.

The surface morphological features of the pure α-Fe_2O_3 and the Li-doped α-Fe_2O_3 samples were examined using SEM and TEM. Fig. 2(a–f) shows SEM images of the pure Fe_2O_3 and the 0.5%, 1%, 2%, 4%, and 6% Li-doped α-Fe_2O_3 samples, respectively, and the insets show the corresponding higher magnification images. All SEM images clearly indicate the deposition of uniform and interconnected nanoparticles (NPs) on the surface of the α-Fe_2O_3 samples. The average particle size of the optimized 0.5% Li-doped α-Fe_2O_3 sample was 50–80 nm. The smaller and porous NPs are believed more surface area, which helps to accelerate ion transformation and is useful for enhancing the electrochemical properties.

Fig. 3(a–c) presents TEM images of the optimized 0.5% Li-doped α-Fe_2O_3 sample obtained at different magnifications, respectively. The TEM results clearly show the development of highly mesoporous and interconnected NPs on the surface of the 0.5% Li-doped α-Fe_2O_3 samples. At higher magnifications, a highly porous layer can be observed on the spherical surface of the NPs (as shown in the marked area with dotted lines in Fig. 3c). Such surface morphology simplifies ion transformation. Moreover, the images show lattice fringes with an interplanar distance of 0.28 nm, which corresponds to the (104) *hkl* plane of α-Fe_2O_3. The selected area electron diffraction patterns in Fig. 3d show the diffraction planes (*hkl*) of pure α-Fe_2O_3, which is consistent with the XRD data, thus confirming the crystalline nature of the 0.5% Li-doped α-Fe_2O_3 sample.

The BET specific surface area of pure α-Fe_2O_3 and optimized 0.5% Li-doped α-Fe_2O_3 samples were determined by N_2 adsorption/desorption measurement. Fig. 4(a–b) shows N_2 adsorption-desorption isotherms of α-Fe_2O_3 and optimized 0.5% Li-doped α-Fe_2O_3 samples and inset of corresponding pore size distributions (nm). For all the samples, the isotherms show a discrete hysteresis loop starting from P/P_o ~0.045 and demonstrate the presence of mesopores. The corresponding pore size distributions were calculated from the desorption part of the isotherms and given in the insets of Fig. 4(a–b). The wide range distribution of mesopores is observed indicating the coexistence of structural pores as well as interconnected pores [19]. The measured Brunauer-Emmett-Teller (BET) values are 98.27 and 148.07 m^2/g for the pure α-Fe_2O_3 and 0.5% Li-doped α-Fe_2O_3. From these observations, it can be concluded that the 0.5% Li-doped α-Fe_2O_3 nanostructure exhibits relatively high BET surface area than that of samples pure α-Fe_2O_3. This is probably due to the open pores formed by the nanoparticles in the 0.5% Li-doped α-Fe_2O_3 (also evident from the TEM results), resulting in a high surface area. The BET results indicate that the substitution of Li into α-Fe_2O_3 greatly enhances the surface area and therefore improves the capacitive performance of the composite electrode effectively [44].

The as-synthesized pure α-Fe_2O_3 and the 0.5%, 1%, 2%, 4%, and 6% Li-doped α-Fe_2O_3 electrodes prepared using the hydrothermal method were subjected to electrochemical testing. All of these electrodes were examined using a three-electrode system in 3 M KOH as the electrolyte; the prepared α-Fe_2O_3 and Li-doped α-Fe_2O_3 electrodes were employed as the working electrodes in this system in the potential range of − 0.1–0.5 V. Figs. 5a and 5b present the CV measurement results and the Cs values of the as-synthesized pure α-Fe_2O_3 and the 0.5%, 1%, 2%, 4%, and 6% Li-doped α-Fe_2O_3 electrodes at a constant scan rate of 100 mV s^{-1}, respectively. The CV curves and their integral areas indicate that the electrochemical properties of 0.5% Li-doped α-Fe_2O_3 are superior to those of α-Fe_2O_3 doped with other Li concentrations and the as-synthesized pure α-Fe_2O_3. Therefore, the Cs of the 0.5% Li-doped α-Fe_2O_3 electrode was higher than those of the other electrodes. The Cs values of pure α-Fe_2O_3 and 0.5%, 1%, 2%, 4%, and 6% Li-doped α-Fe_2O_3 were 52, 79, 30, 24, 21, and 12 mAh g^{-1}, respectively. These Cs values indicate that the electrical properties of the 0.5% Li-doped α-Fe_2O_3 were enhanced, which means that Li^+ replaced Fe^{3+} ions. Moreover, owing to the smaller-sized NPs comprising the 0.5% Li-doped α-Fe_2O_3 electrode, its surface area was larger and porosity higher, which increased its Cs value [51].

Fig. 5(c, d) and Fig. S1 (a–d) show the CV curves of pure α-Fe_2O_3 and Li-doped α-Fe_2O_3 (0.5%, 1%, 2%, 4%, and 6%) obtained at scan rates of 5–100 mV s^{-1}, respectively. All CV curves show the formation of stronger redox and oxidation peaks, and the peaks are shifted toward the positive and negative potential window, indicating the occurrence of faster Faradaic reactions between Li^+ and Fe^{3+} ions. The Cs values of the pure α-Fe_2O_3 and Li-doped α-Fe_2O_3 (0.5%, 1%, 2%, 4%, and 6%) at scan rates of 5–100 mV s^{-1} (as shown in Fig. 5e), respectively, indicate that the Cs values of the 0.5% Li-doped α-Fe_2O_3 electrode were the highest. The Cs values of the optimized 0.5% Li-doped α-Fe_2O_3 electrode at the various scan rates in the range of 5–100 mV s^{-1} were 79, 76, 73, 55, 43, and 73 mAh g^{-1}. The CV curves and the integral area are higher than those of the other electrodes, indicating that the 0.5% Li-doped α-Fe_2O_3 is useful for the enhanced electrical properties in comparison with the α-Fe_2O_3 nanomaterials. The Cs values of the 0.5% Li-doped α-Fe_2O_3 composite were significantly higher than those of the pure α-Fe_2O_3 and other Li-doped α-Fe_2O_3 electrodes at various scan rates, indicating a positive synergic effect between pure α-Fe_2O_3 and 0.5% Li doping. Fig. 5d shows the CV curves of the 0.5% Li-doped α-Fe_2O_3 electrode at different scan rates of 5–100 mV s^{-1} in the same potential window. According to Fig. 5e, the Cs value of the final 0.5% Li-doped α-Fe_2O_3 composite is 79 mAh g^{-1} at a constant scan rate of 5 mV s^{-1}, which is considerably higher than that of pure α-Fe_2O_3 (52 mAh g^{-1}) and 1% Li-doped α-Fe_2O_3 (30 mAh g^{-1}), 2% Li-doped α-Fe_2O_3 (24 mAh g^{-1}), 4% Li-doped α-Fe_2O_3 (21 mAh g^{-1}), and 6% Li-doped α-Fe_2O_3 (12 mAh g^{-1}) at the same scan rate. The outstanding improvement in the Cs of the 0.5% Li-doped Fe_2O_3 composite electrode can be attributed to the higher conductivity of the porous nanoparticles and the positive synergic effect [51–53]. The previously reported values of the supercapacitors are summarized in Table S1, indicating that Li doping in Fe_2O_3 materials is a superior alternative option for supercapacitor testing to the other dopants.

To the authors' knowledge, the literature contains few reports on metal-doped iron oxide NPs for use in supercapacitor applications. For example, Dubal et al. [55] prepared the Fe-doped nanomaterial for the supercapacitor application. They mentioned that after the 2% Fe doping in the MnO_2, electrodes show more supercapacitor performance than the pristine MnO_2. Kulal et al. [56] synthesized Fe_2O_3 thin films using the SILAR method for the supercapacitor properties. They observed that the Fe_2O_3 shows an amorphous crystal structure. Finally, they reported the prepared Fe_2O_3 electrode exhibited the Cs

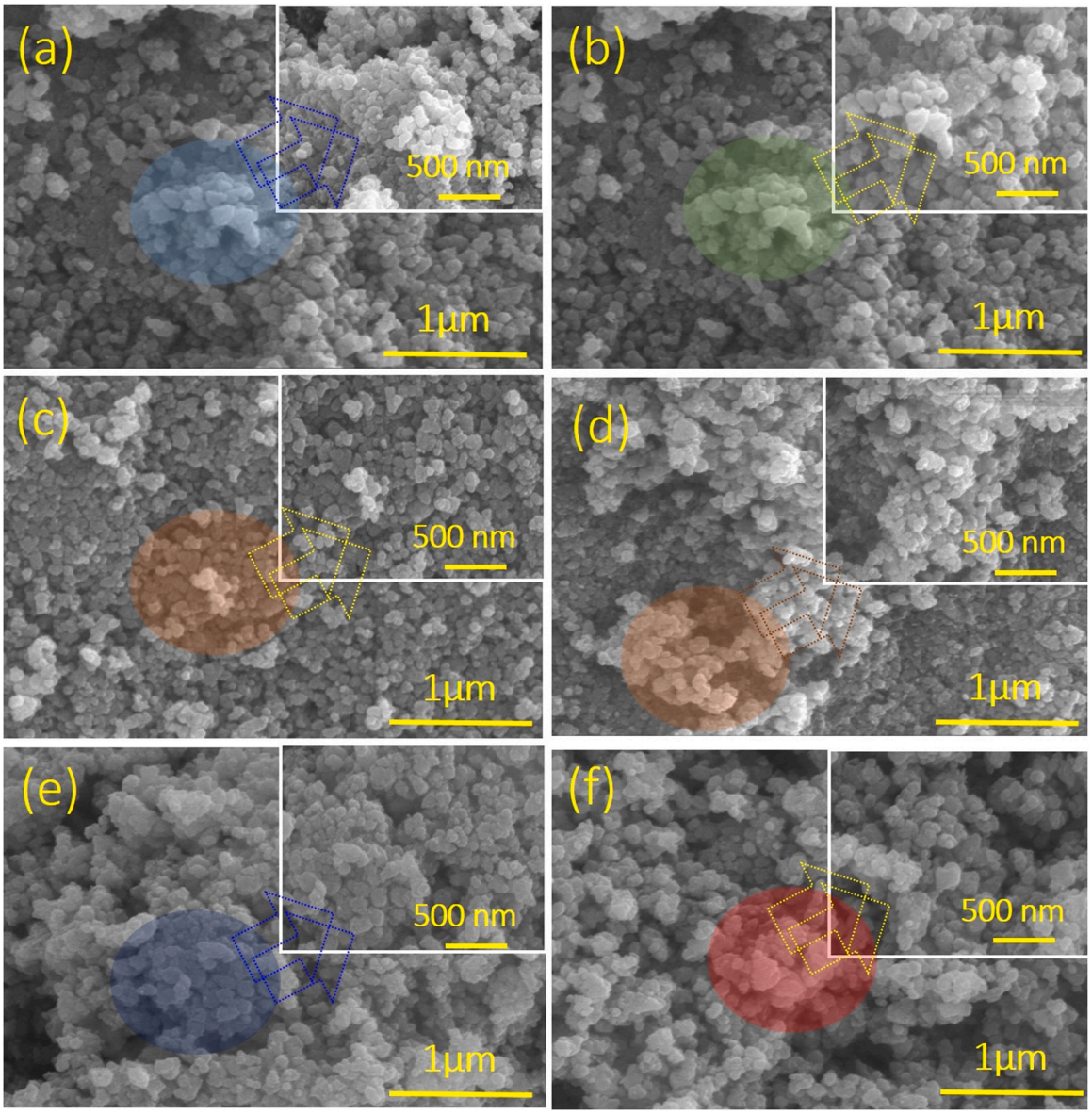

Fig. 2. (a–f) SEM images of the pure α-Fe_2O_3 and Li doped α-Fe_2O_3 prepared at a different percentage of Li (0.5%, 1%, 2%, 4%, and 6%, respectively), inset shows the higher magnifications images, respectively.

of 178 F g^{-1} at the lower scan rate of 5 mV s^{-1} in the 1 M NaOH electrolyte. For this reason, we developed novel nanomaterials (0.5% Li-doped α-Fe_2O_3) with good stability for use in supercapacitor applications, which was hitherto not attempted. Fig. 5f shows the cycling retention capacity of the pure α-Fe_2O_3 and the optimized 0.5% Li-doped α-Fe_2O_3 electrodes at the constant current density 2 mA cm^{-2} up to 3000 cycles in the same potential window. The α-Fe_2O_3 and optimized 0.5% Li-doped α-Fe_2O_3 electrodes exhibited cycling retentions of 89% and 96% up to 3000 cycles, indicating the superiority of the 0.5% Li-doped α-Fe_2O_3 electrode over the pure α-Fe_2O_3 electrode.

Similarly, the GCD curves of the pure as-synthesized α-Fe_2O_3 electrode and the electrodes made of α-Fe_2O_3 doped with different percentages of Li (0.5%, 1%, 2%, 4%, and 6%) were tested at a constant current density of 1 mA cm^{-2} in a potential window of 0–0.5 V (as shown in Fig. 6a). The GCD curves indicate that the charge-discharge times were 33.55, 48.02, 40.12, 34.72, 31.94, and 13.67 s for the pure α-Fe_2O_3 and 0.5%, 1%, 2%, 4%, and 6% Li-doped α-Fe_2O_3 electrodes, respectively. Moreover, the Ir drop (0.021 V) of the 0.5% Li-doped α-Fe_2O_3 sample was considerably lower than those of the others, which indicates that the Cs value of the 0.5% Li-doped electrode is higher. According to the GCD shapes and recorded discharge times (s), that discharge time of the 0.5% Li-doped α-Fe_2O_3 electrode was longer than those of the pure and other Li-doped α-Fe_2O_3 electrodes, which indicates that this electrode has the highest Cs, as illustrated in Fig. 6d.

Fig. 6(b, c) and Fig. S2 (a–d) show the GCD curves of the pure α-Fe_2O_3, optimized 0.5% Li-doped α-Fe_2O_3, and other Li-doped α-Fe_2O_3 electrodes for current densities of 1–5 mA cm^{-2}, respectively. All of the results in these Figures (Fig. 6 and S2) indicate that the final 0.5% Li-doped α-Fe_2O_3 composite electrode had a higher Cs than those of the other electrodes. Fig. 6d shows the Cs values of pure α-Fe_2O_3, optimized 0.5% Li-doped Fe_2O_3, and other Li-doped α-Fe_2O_3 composite electrodes at current densities of 1–5 mA cm^{-2}. The Cs values of the pure α-Fe_2O_3, 0.5% Li-doped α-Fe_2O_3, 1% Li-doped α-Fe_2O_3, 2% Li-doped α-Fe_2O_3, 4% Li-doped α-Fe_2O_3, and 6% Li-doped α-Fe_2O_3 composite electrodes are 38, 43, 39, 34, 31, and 24 mAh g^{-1}, respectively, at a constant current density of 1 mA cm^{-2}. These resultant Cs values suggest that the final 0.5% Li-doped α-Fe_2O_3 composite electrode is superior to all the other prepared electrodes

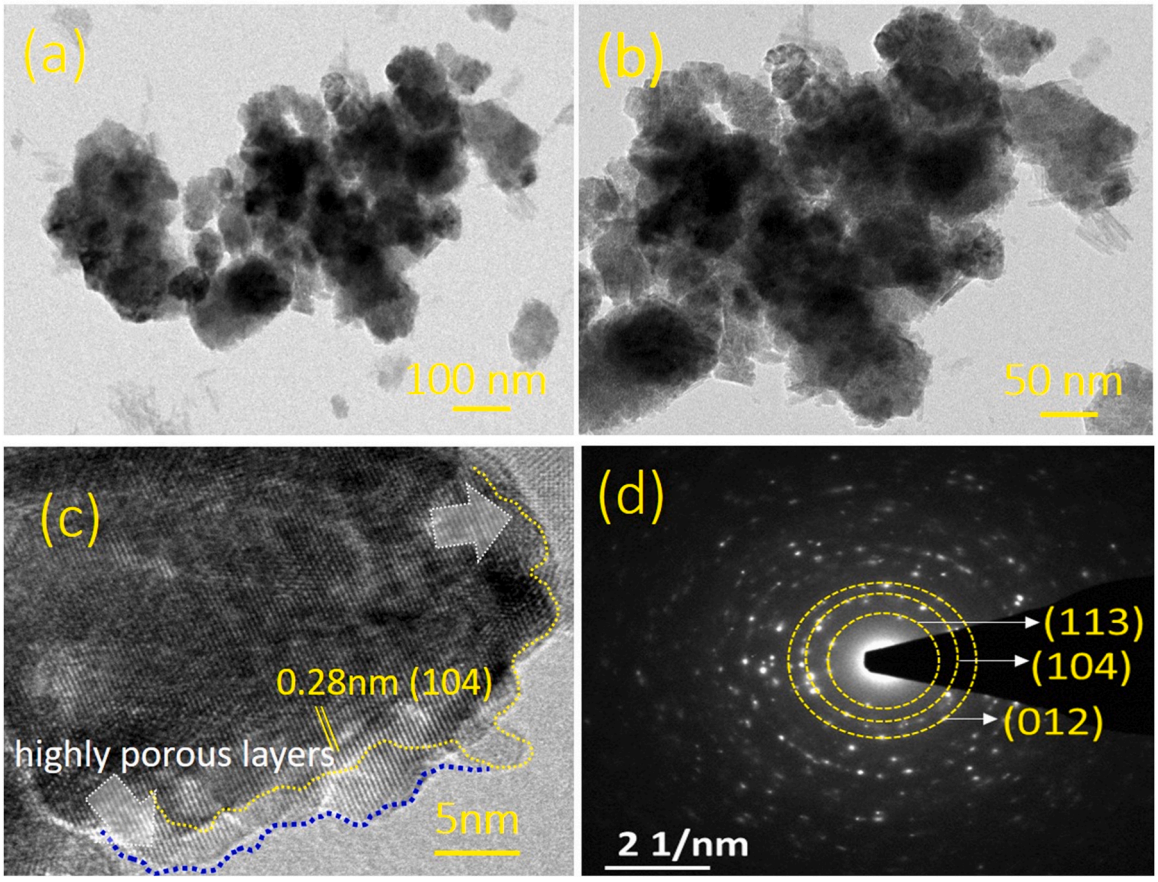

Fig. 3. (a-c) TEM images with different magnifications of the optimized 0.5% Li doped α-Fe_2O_3 sample, respectively, (d) SEAD pattern of the optimized 0.5% Li doped α-Fe_2O_3 sample.

because of the growth of a porous and uniform LiO layer on the α-Fe_2O_3 NPs, which is useful for accelerating the Faradaic reactions to realize the enhanced electrochemical properties required in various supercapacitor applications [54]. The Cs values of the final composite 0.5% Li-doped α-Fe_2O_3 electrode were 43, 38, 36, 34, and 31 mAh g^{-1} for the current densities of 1–5 mA cm^{-2}, respectively. These results indicate that the 0.5% Li-doped α-Fe_2O_3 electrode was considerably more suited for use in supercapacitor applications owing to its interconnected and porous NP-like nanostructures that accelerate ion transfer and its porous surface that provides a higher level of electrical conductivity [51,54].

To examine the standard working mechanism of the synthesized working electrode in aqueous electrolyte (KOH), we performed EIS measurements at 1–100 kHz in 3 M aqueous KOH. Fig. 7 presents a comparative study of the Nyquist plots of the pure α-Fe_2O_3, 0.5% Li-doped α-Fe_2O_3, 1% Li-doped α-Fe_2O_3, 2% Li-doped α-Fe_2O_3, 4% Li-doped α-Fe_2O_3, and 6% Li-doped α-Fe_2O_3 composite electrodes. Table 1 lists the solution resistance (R_s) and charge-transfer

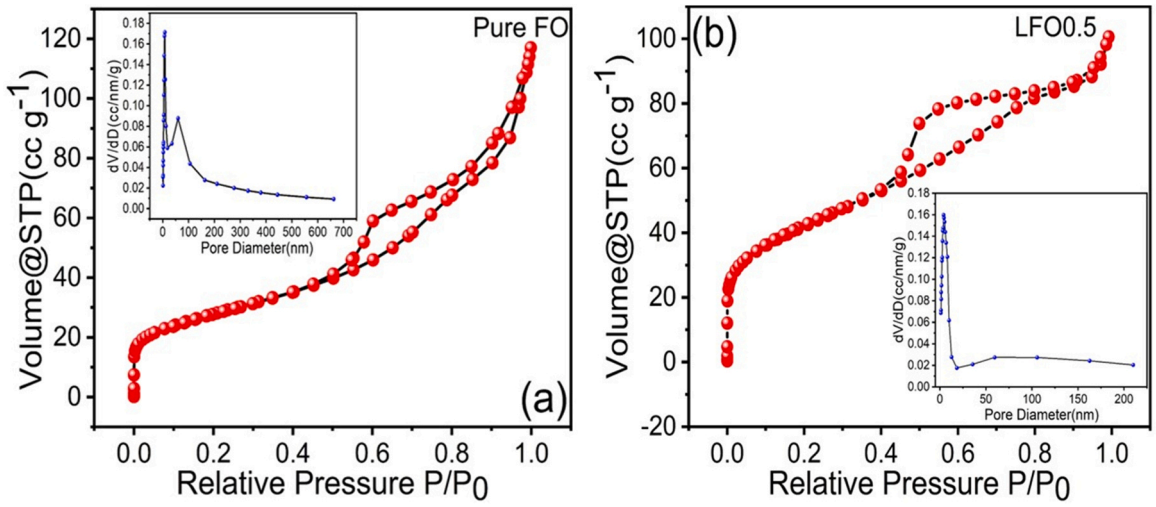

Fig. 4. Nitrogen adsorption and desorption isotherms of (a) pure α-Fe_2O_3 and (b) optimized 0.5% Li doped α-Fe_2O_3 and the insets show the corresponding BJH pore distributions size.

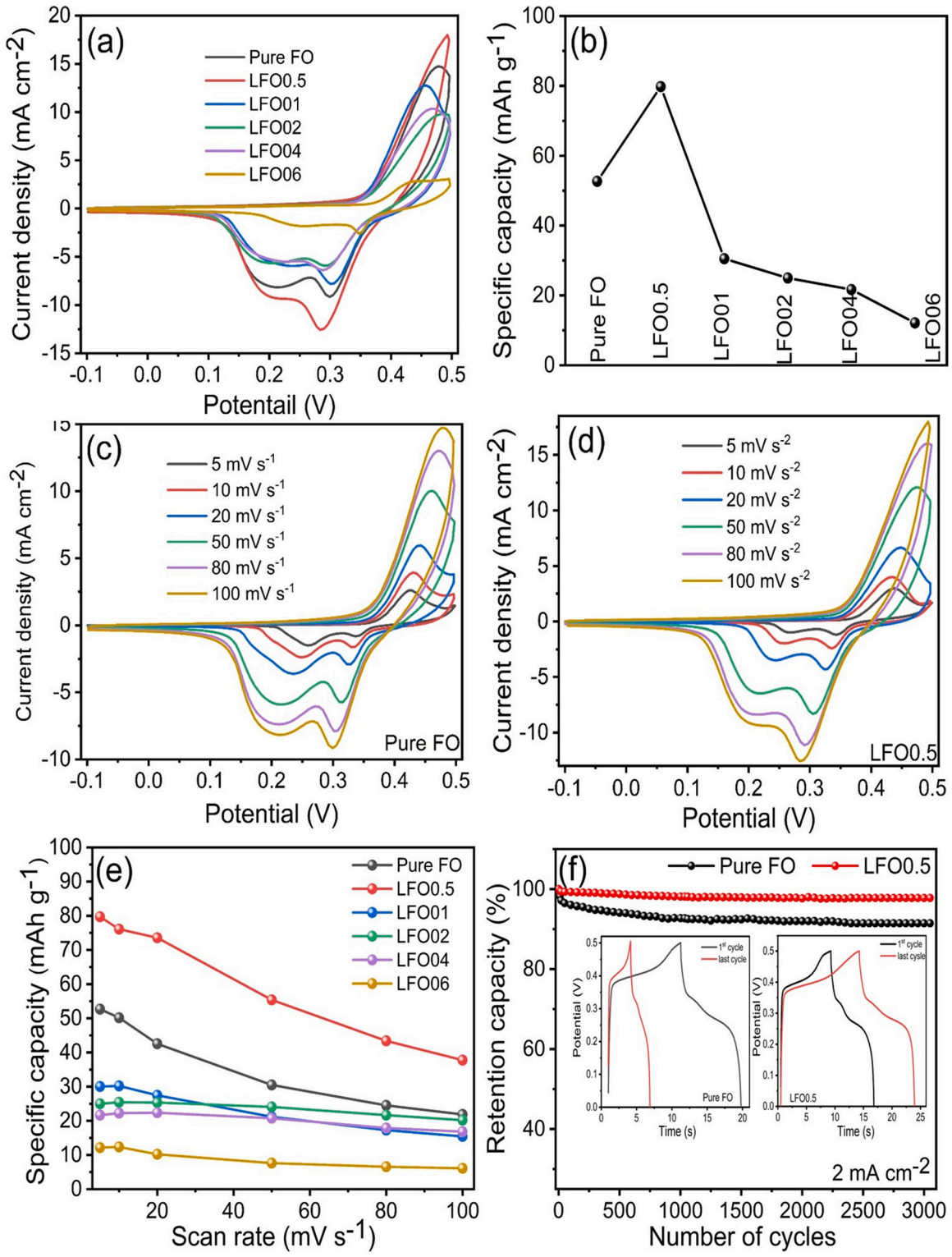

Fig. 5. (a) CV curves the pure α-Fe_2O_3 and Li doped α-Fe_2O_3 at constant scan rates 100 mV s^{-1} (b) specific capacity of the pure α-Fe_2O_3 and Li doped α-Fe_2O_3 at constant scan rate 100 mV s^{-1}, (c, d) CV curves of pure α-Fe_2O_3 and optimized 0.5% Li doped α-Fe_2O_3 electrodes at different scan rates from 5 to 100 mV s^{-1}, (e) specific capacity of the pure α-Fe_2O_3 and Li doped α-Fe_2O_3 prepared at a different percentage of Li (0.5%, 1%, 2%, 4%, and 6%, respectively) with various scan rates, (f) cycling stability of the pure α-Fe_2O_3 and optimized 0.5% Li doped α-Fe_2O_3 electrodes up to 3000 cycles.

resistance (R_{ct}) values of all electrodes. The calculated R_{ct} value of 2.47 Ω for the 0.5% Li-doped Fe_2O_3 composite electrode is considerably lower than that of the pure α-Fe_2O_3 electrode, as well as those of the 1% Li-doped α-Fe_2O_3, 2% Li-doped α-Fe_2O_3 , 4% Li-doped α-Fe_2O_3, and 6% Li-doped α-Fe_2O_3 composite electrodes. The R_s and R_{ct} of the 0.5% Li-doped α-Fe_2O_3 composite electrode are 1.98 Ω and 2.47 Ω, respectively. The calculated R_s and R_{ct} values are lower than those of the other electrodes, which indicates that the 0.5% Li-doped composite has higher Cs and is appropriate for the electrochemical applications.

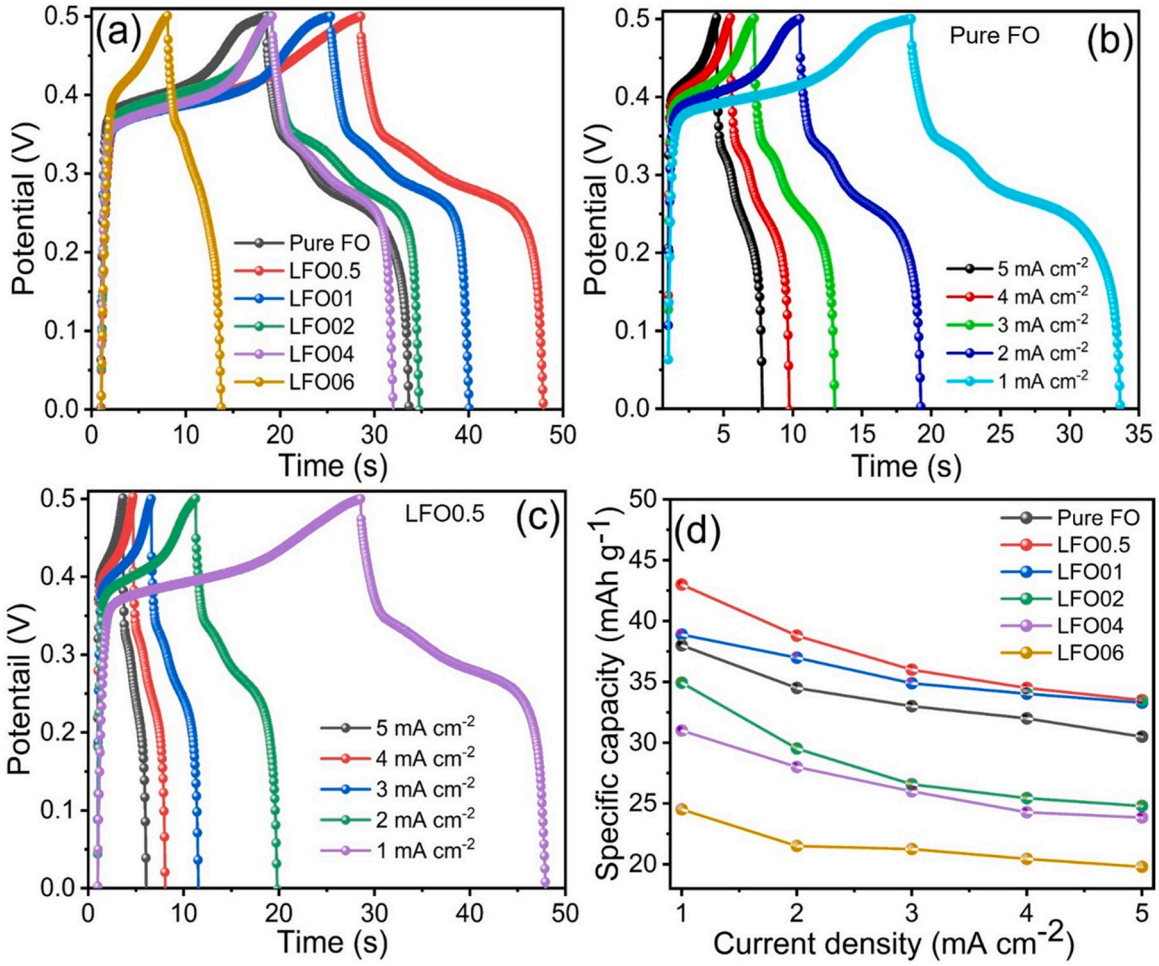

Fig. 6. (a) GCD curves the pure α-Fe_2O_3 and Li doped α-Fe_2O_3 at a constant current density 1 mA cm^{-2}, (b, c) GCD curves of pure α-Fe_2O_3 and optimized 0.5% Li doped α-Fe_2O_3 electrodes at different current densities from 1 to 5 mA cm^{-2}, (d) specific capacity of the pure α-Fe_2O_3 and Li doped α-Fe_2O_3 prepared at a different percentage of Li (0.5%, 1%, 2%, 4%, and 6%, respectively) with various current densities, respectively.

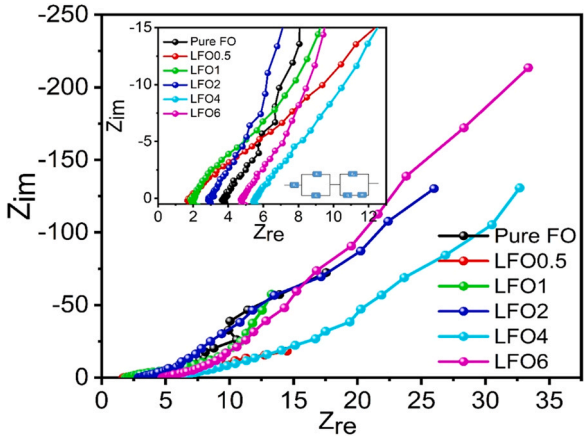

Fig. 7. Nyquist plots of the pure α-Fe_2O_3 and Li doped α-Fe_2O_3 electrodes at a different doping percentage of the Li, inset shows the zoom area of the Nyquist plot and equivalent circuit.

3.1. Hybrid supercapacitor application

To cheek practical applicative of the as-prepared 0.5% Li doped α-Fe_2O_3 electrode, we constructed asymmetric hybrid supercapacitors of 0.5% Li doped α-Fe_2O_3//AC (LFO0.5//AC) device, as prepared 0.5% Li doped α-Fe_2O_3 electrodes as a positive electrode, AC as a negative electrode, and 0.5 M KOH/PVA electrolyte gel, respectively. Fig. 8a shows the CV curves of the asymmetric hybrid supercapacitors of the LFO0.5//AC electrode with various potential windows at a constant scan rate of 50 mV s^{-1}, respectively. The CV curves indicate that 1.5 V shows a higher surface area compared to the other potential windows, therefore we finalized 1.5 V for further electrochemical study. Fig. 8b shows the CV curves of the asymmetric hybrid supercapacitors of the LFO0.5//AC electrode with different scan rates of 5–100 mV s^{-1}, at a constant potential window, respectively. The CV curves of the device show strong reduction and oxidation peaks at 0.3 V and 0.8 V, which indicates the faradic reaction occurred during the electrochemical reaction. Similarly, the optimization of the potential window. Fig. 8c shows the GCD curves of the asymmetric hybrid supercapacitors of the LFO0.5//AC electrode with different potential windows from 0.9 to 1.7 V at a constant current density, respectively. The GCD curves at different potential windows indicate

Table 1
The calculated EIS parameters of pure α-Fe_2O_3, Li doped α-Fe_2O_3 at a different percentage of Li(0.5%, 1%, 2%, 4%, and 6%) composite electrodes.

Sample ID	$R_s(\Omega)$	$R_{ct}(\Omega)$
Pure FO	2.91	12.26
LFO0.5	1.98	2.47
LFO01	3.76	2.96
LFO02	3.19	8.97
LFO04	4.74	18.86
LFO06	5.46	18.11

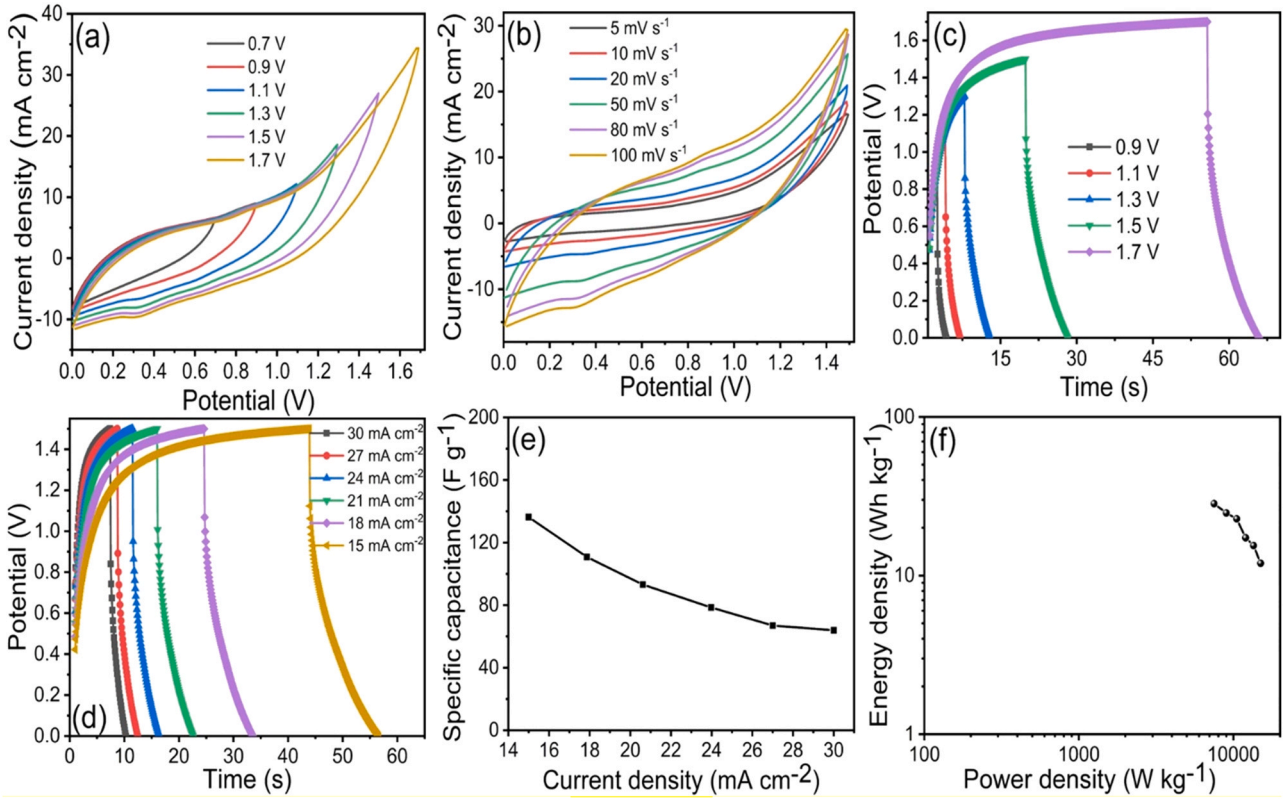

Fig. 8. (a) CV of the 0.5% Li doped α-Fe_2O_3//AC at different potential windows at constant scan rates 100 mV s^{-1}, (b) CV of the 0.5% Li doped α-Fe_2O_3//AC at different scan rates from 5 to 100 mV s^{-1} with constant potential window 1.5 V, (c) GCD of the 0.5% Li doped α-Fe_2O_3//AC at different potential windows at constant current density, (d) GCD of the 0.5% Li doped α-Fe_2O_3//AC at different current densities from 15 to 30 mA cm^{-2} with constant potential window 1.5 V, (e) Cs of the 0.5% Li doped α-Fe_2O_3//AC device, (f) Ragone plots of the 0.5% Li doped α-Fe_2O_3//AC device, respectively.

that 1.5 V is the better potential window for further electrochemical study. Fig. 8d shows the GCD curves of the asymmetric hybrid supercapacitors of the LFO0.5//AC electrode with different current densities from 15 to 30 mA cm^{-2} at a constant potential window of 1.5 V respectively. Fig. 8e shows the calculated Cs values of the LFO0.5//AC electrode with different current densities, respectively. The obtained values of the Cs of the LFO0.5//AC electrode is 136 F g^{-1} at a current density of 15 mA cm^{-2}. The calculated values of the LFO0.5//AC device are superior to the previously reported results [57,58]. Another important parameter is Ragone plots as shown in Fig. 8f. The asymmetric hybrid supercapacitor of the LFO0.5//AC cell provided the power density and energy density of 7508 W kg^{-1} and 28.73 Wh kg^{-1}, respectively. EIS results indicate the lower resistivity and higher electrical conductivity of the hybrid asymmetric supercapacitor of the LFO0.5//AC cell (as shown in Fig. S3). These electrochemical properties of the Li-doped α-Fe_2O_3 composite electrode show that the Li doping in binary iron oxide is a promising electrode material for the electrochemical application and next generation of hybrid supercapacitor energy storage devices.

4. Conclusions

In brief, we summarized the current research work on the Li-doped α-Fe_2O_3 via a simple and easy hydrothermal reaction method for supercapacitor application. The structural and morphological features were analyzed by various characterization techniques such as XRD, XPS, SEM, and TEM respectively. The surface morphological results show the uniform deposition of NPs-like nanostructure grows on the surface of Fe_2O_3 materials. In comparison with pure Fe_2O_3, 0.5% Li doped α-Fe_2O_3 demonstrates outstanding electrochemical performance in an alkaline medium. The electrochemical results indicate the 0.5% Li doped α-Fe_2O_3 electrode shows enhanced values for Cs than the pure α-Fe_2O_3 and other Li doping percentage samples, suggesting that the 0.5% Li doped α-Fe_2O_3 will be more useful for the further electrochemical study, because of lower particle size, mesoporous nanostructure, and lower values of solution resistance and charge transfer resistance. Furthermore, constructed two-electrode device of the 0.5% Li doped α-Fe_2O_3 sample shows better specific energy of 28.73 Wh kg^{-1} and specific power of 7508 W kg^{-1} with a higher specific capacitance of 136 F g^{-1}.

CRediT authorship contribution statement

AMT: Conceptualization, Methodology, Writing – original draft. **MST**: Data curation. **SKS**: Software, Visualization, Investigation. **JHB**: Software. **NTNT**: Software, Validation. **CHK**: Supervision. **CHP**: Supervision, Writing – review & editing.

Data availability

Data will be made available on request.

Declaration of Competing Interest

The authors declare that they have no known competing financial interests or personal relationships that could have appeared to influence the work reported in this paper.

Acknowledgements

This work was supported by the KENTECH Research Grant (KRG 2021-01-008).

Appendix A. Supporting information

Supplementary data associated with this article can be found in the online version at doi:10.1016/j.jallcom.2022.167242.

References

[1] P.P. Simon, Y. Gogotsi, B. Dunn, Where do batteries end and supercapacitors begin? Science 343 (2014) 1210–1211.
[2] M.R. Lukatskaya, B. Dunn, Y. Gogotsi, Multidimensional materials and device architectures for future hybrid energy storage, Nat. Commun. 7 (2016) 12647.
[3] S.K. Shinde, M.B. Jalak, G.S. Ghodake, N.C. Maile, H.M. Yadav, A.D. Jagadale, Asif Shahzad, D.S. Lee, A.A. Kadam, V.J. Fulari, D.-Y. Kim, Flower-like $NiCo_2O_4$/$NiCo_2S_4$ electrodes on Ni mesh for higher supercapacitor applications, Ceram. Int. 45 (2019) 17192–17203.
[4] S.K. Shinde, M.B. Jalak, S.Y. Kim, H.M. Yadav, G.S. Ghodake, A.A. Kadam, D.-Y. Kim, Effect of Mn doping on the chemical synthesis of interconnected nanoflakes-like CoS thin films for high performance supercapacitor applications, Ceram. Int. 44 (2018) 23102–23108.
[5] M. Winter, R. Brodd, What are batteries, supercapacitors and fuel cells? Chem. Rev. 104 (2004) 4245–4270.
[6] A.M. Tamboli, M.S. Tamboli, C.S. Praveen, P.K. Dwivedi, I. Karbhal, S.W. Gosavi, M.V. Shelke, B.B. Kale, Architecture of $NaFe(MoO_4)_2$ as a novel anode material for rechargeable lithium and sodium ion batteries, Appl. Surf. Sci. 559 (2021) 149903.
[7] M.S. Tamboli, H.S. Jadhav, D.R. Patil, A.F. Shaikh, S.S. Patil, J.G. Seo, H. Choi, S.W. Gosavi, B.B. Kale, Hierarchical novel $NiCo_2O_4$/$BiVO_4$ hybrid heterostructure as an advanced anode material for rechargeable lithium ion battery, Int. J. Energy Res. 44 (2020) 12126–12135.
[8] A.M. Tamboli, M.S. Tamboli, P.K. Dwivedi, C.S. Praveen, I. Karbhal, S.W. Gosavi, M.V. Shelke, B.B. Kale, Engineering microstructure of $LiFe(MoO_4)_2$ as an advanced anode material for rechargeable lithium-ion battery, J. Mater. Sci. Mater. Electron 32 (2021) 24273–24284.
[9] J. Yang, C. Yu, X. Fan, C. Zhao, J. Qiu, Ultrafast self-assembly of graphene oxide-induced monolithic NiCo–carbonate hydroxide nanowire architectures with a superior volumetric capacitance for supercapacitors, Adv. Funct. Mater. 25 (2015) 2109–2116.
[10] Y. Wang, T. Zhou, K. Jiang, P. Da, Z. Peng, J. Tang, B. Kong, W.B. Cai, Z. Yang, G. Zheng, Reduced mesoporous Co_3O_4 nanowires as efficient water oxidation electrocatalysts and supercapacitor electrodes, Adv. Energy Mater. 4 (2014) 1400696.
[11] C. Rao, A. Sood, K. Subrahmanyam, A. Govindaraj, Graphene: the new two-dimensional nanomaterial, Angew. Chem. 48 (2009) 7752–7777.
[12] X. Zhao, B.M. Sánchez, P.J. Dobson, P.S. Grant, The role of nanomaterials in redox-based supercapacitors for next generation energy storage devices, Nanoscale 3 (2011) 839–855.
[13] S.K. Shinde, M.B. Jalak, G.S. Ghodake, N.C. Maile, V.S. Kumbhar, D.S. Lee, V.J. Fulari, D.-Y. Kim, Chemically synthesized nanoflakes-like $NiCo_2S_4$ electrodes for high-performance supercapacitor application, Appl. Surf. Sci. 466 (2019) 822–829.
[14] Y. Ji, L. Huang, J. Hu, C. Streb, Y.F. Song, Polyoxometalate-functionalized nanocarbon materials for energy conversion, energy storage and sensor systems, Energy Environ. Sci. 8 (3) (2015) 776–789.
[15] H.M. Yadav, G.S. Ghodake, D.-Y. Kim, Sivalingam Ramesh, N.C. Maile, D.S. Lee, S.K. Shinde, Nanorods to hexagonal nanosheets of CuO-doped manganese oxide nanostructures for higher electrochemical supercapacitor performance, Colloids Surf. B 184 (2019) 110500.
[16] S.K. Shinde, S.M. Mohite, A.A. Kadam, H.M. Yadav, G.S. Ghodake, K.Y. Rajpure, D.S. Lee, D.-Y. Kim, Effect of deposition parameters on spray pyrolysis synthesized CuO nanoparticle thin films for higher supercapacitor performance, J. Electroanal. Chem. 850 (2019) 113433.
[17] S.S. Patil, D.P. Dubal, V.G. Deonikar, M.S. Tamboli, J.D. Ambekar, P. Gomez-Romero, S.S. Kolekar, B.B. Kale, D.R. Patil, Fern-like rGO/$BiVO_4$ hybrid nanostructures for high-energy symmetric supercapacitor, ACS Appl. Mater. Interfaces 8 (46) (2016) 31602–31610.
[18] S.S. Patil, D.P. Dubal, M.S. Tamboli, J.D. Ambekar, S.S. Kolekar, Ag: $BiVO_4$ dendritic hybrid-architecture for high energy density symmetric supercapacitors, J. Mater. Chem. A 4 (20) (2016) 7580–7584.
[19] M.S. Tamboli, D.P. Dubal, S.S. Patil, A.F. Shaikh, V.G. Deonikar, M.V. Kulkarni, N.N. Maldar, A.M. Asiri, P. Gomez-Romero, B.B. Kale, D.R. Patil, Mimics of microstructures of Ni substituted $Mn_{1-x}Ni_xCo_2O_4$ for high energy density asymmetric capacitors, Chem. Eng. J. 307 (2017) 300–310.
[20] S. Kumar, M.A. Rehman, S. Lee, M. Kim, H. Hong, J.Y. Park, Y. Seo, Supercapacitors based on Ti_3C_2TxMXene extracted from supernatant and current collectors passivated by CVD-graphene, Sci. Rep. 11 (2021) 1–9.
[21] T. Wang, H.C. Chen, F. Yu, X.S. Zhao, H. Wang, Boosting the cycling stability of transition metal compounds-based supercapacitors, Energy Storage Mater. 16 (2019) 545–573.
[22] O. Sadak, W. Wang, J. Guan, A.K. Sundramoorthy, S. Gunasekaran, MnO_2 nanoflowers deposited on graphene paper as electrode materials for supercapacitors, ACS Appl. Nano Mater. 2 (7) (2019) 4386–4394.
[23] S.H. Yi, H.C. Lin, M.J. Chen, Ultra-high energy storage density and scale-up of antiferroelectric TiO_2/ZrO_2/TiO_2 stacks for supercapacitors, J. Mater. Chem. 9 (14) (2021) 9081–9091.
[24] S. Jeon, J.H. Jeong, H. Yoo, H.K. Yu, B.H. Kim, M.H. Kim, RuO_2 nanorods on electrospun carbon nanofibers for supercapacitors, ACS Appl. Nano Mater. 3 (4) (2020) 3847–3858.
[25] C. Wu, Z. Zhang, Z. Chen, Z. Jiang, H. Li, H. Cao, Y. Liu, Y. Zhu, Z. Fang, X. Yu, Rational design of novel ultra-small amorphous Fe_2O_3 nanodots/graphene heterostructures for all-solid-state asymmetric supercapacitors, Nano Res. 14 (4) (2021) 953–960.
[26] F.N. Tuzluca, Y.O. Yesilbag, M. Ertugrul, Synthesis of In_2O_3 nanostructures with different morphologies as potential supercapacitor electrode materials, Appl. Surf. Sci. 427 (2018) 956–964.
[27] N.C. Maile, M. Moztahida, A.A. Ghani, M. Hussain, K. Tahir, B. Kim, S.K. Shinde, V.J. Fulari, D.S. Lee, Electrochemical synthesis of binder-free interconnected nanosheets of Mn-doped Co_3O_4 on Ni foam for high-performance electrochemical energy storage application, Chem. Eng. J. 421 (2021) 129767.
[28] W. Lu, Y. Li, M. Yang, X. Jiang, Y. Zhang, Y. Xing, Construction of hierarchical Mn_2O_3@MnO_2 core-shell nanofibers for enhanced performance supercapacitor electrodes, ACS Appl. Energy Mater. 3 (9) (2020) 8190–8197.
[29] J. Jiang, Y. Li, J. Liu, X. Huang, C. Yuan, X.W. Lou, Recent advances in metal oxide-based electrode architecture design for electrochemical energy storage, Adv. Mater. 24 (38) (2012) 5166–5180.
[30] V.D. Nithya, N.S. Arul, Review on α- Fe_2O_3 based negative electrode for high-performance supercapacitors, J. Power Sources 327 (2016) 297–318.
[31] Y. Zeng, M. Yu, Y. Meng, P. Fang, X. Lu, Y. Tong, Iron based supercapacitor electrodes: advances and challenges, Adv. Energy Mater. 6 (2016) 1601053.
[32] C. Guan, J. Liu, Y. Wang, L. Mao, Z. Fan, Z. Shen, H. Zhang, J. Wang, Iron oxide-decorated carbon for supercapacitor anodes with ultrahigh energy density and outstanding cycling stability, ACS Nano 9 (2015) 5198–5207.
[33] C. Guan, W. Zhao, Y. Hu, Q. Ke, X. Li, H. Zhang, J. Wang, High-performance flexible solid-state Ni/Fe battery consisting of metal oxides coated carbon cloth/carbon nanofiber electrodes, Adv. Energy Mater. 6 (2016) 1601034.
[34] K.K. Lee, S. Deng, H.M. Fan, S. Mhaisalkar, H.R. Tan, E.S. Tok, K.P. Loh, W.S. Chin, C.H. Sow, α-Fe_2O_3 nanotubes reduced graphene oxide composites as synergistic electrochemical capacitor materials, Nanoscale 4 (2012) 2958–2961.
[35] H. Zhang, Q. Gao, K. Yang, Y. Tan, W. Tian, L. Zhu, Z. Li, C. Yang, Solvothermally induced α-Fe_2O_3/graphene nanocomposites with ultrahigh capacitance and excellent rate capability for supercapacitors, J. Mater. Chem. 3 (2015) 22005–22011.
[36] L. Wang, H. Yang, X. Liu, R. Zeng, M. Li, Y. Huang, X. Hu, Constructing hierarchical tectorum-like α-Fe_2O_3/PPy nanoarrays on carbon cloth for solid-state asymmetric supercapacitors, Angew. Chem. 56 (2017) 1105–1110.
[37] J.Q. Liu, M.B. Zheng, X.Q. Shi, H.B. Zeng, H. Xia, Amorphous FeOOH quantum dots assembled mesoporous film anchored on graphene nanosheets with superior electrochemical performance for supercapacitors, Adv. Funct. Mater. 26 (2016) 919–930.
[38] Z.H. Chen, J.D. Chen, F.X. Bu, P.O. Agboola, I. Shakir, Y.X. Xu, Double-holey-heterostructure frameworks enable fast, stable, and simultaneous ultrahigh gravimetric, areal, and volumetric lithium storage, ACS Nano 12 (2018) 12879–12887.
[39] S.Y. Kim, T.Y. Yun, K.S. Yu, H.C. Moon, Reliable, high-performance electrochromic supercapacitors based on metal-doped nickel oxide, ACS Appl. Mater. Interfaces 12 (46) (2020) 51978–51986.
[40] K. Karthikeyan, S. Amaresh, S.N. Lee, V. Aravindan, Y.S. Lee, Fluorine-doped Fe_2O_3 as high energy density electroactive material for hybrid supercapacitor applications, Chem. Asian J. 9 (3) (2014) 852–857.
[41] S. Asaithambi, P. Sakthivel, M. Karuppaiah, G.U. Sankar, K. Balamurugan, R. Yuvakkumar, M. Thambidurai, G. Ravi, Investigation of electrochemical properties of various transition metals doped SnO_2 spherical nanostructures for supercapacitor applications, J. Energy Storage 31 (2020) 101530.
[42] R. Dong, Q. Ye, L. Kuang, X. Lu, Y. Zhang, X. Zhang, G. Tan, Y. Wen, F. Wang, Enhanced supercapacitor performance of Mn_3O_4 nanocrystals by doping transition-metal ions, ACS Appl. Mater. Interfaces 5 (2013) 9508–9516.
[43] Y. Wang, M. Zhang, D. Pan, Yuan Li, T. Ma, J. Xie, Nitrogen/sulfur co-doped graphene networks uniformly coupled N-Fe2O3 nanoparticles achieving enhanced supercapacitor performance, Electrochim. Acta 266 (2018) 242–253.
[44] S.K. Shinde, D.P. Dubal, G.S. Ghodake, P. Gomez-Romero, S. Kim, V.J. Fulari, Influence of Mn incorporation on the supercapacitive properties of hybrid CuO/Cu (OH) 2 electrodes, RSC Adv. 5 (39) (2015) 30478–30484.
[45] U.M. Chougale, V.J. Fulari, Facile synthesis of maghemite nanoflakes arrays for supercapacitor application, Mater. Sci. Semicond. Process. 27 (2014) 682–688.
[46] S. Luo, J. Li, J. Lu, F. Tao, J. Wan, B. Zhang, X. Zhou, C. Hu, High-performance aqueous asymmetric supercapacitor based on hierarchical wheatear-like $LiNi_{0.5}Mn_{1.5}O_4$ cathode and porous Fe_2O_3 anode, Mater. Today Phys. 17 (2021) 100337.
[47] Y. Wang, Y. Zhang, T.C. Zhang, G. Xiang, X. Wang, S. Yuan, Removal of trace arsenite through simultaneous photocatalytic oxidation and adsorption by magnetic Fe_3O_4@ PpPDA@ TiO_2 core–shell nanoparticles, ACS Appl. Nano Mater. 3 (8) (2020) 8495–8504.
[48] Y. Ma, J. Yang, Y.K. Yuan, H. Zhao, Q. Shi, F.J. Zhang, C.J. Pei, B. Liu, H.Q. Yang, Enhanced gas sensitivity and sensing mechanism of network structures assembled from α-Fe_2O_3 nanosheets with exposed {104} facets, Langmuir 33 (2017) 8671.
[49] F. Strauß, E. Hüger, P. Heitjans, V. Trouillet, M. Bruns, H. Schmidt, Li–Si thin films for battery applications produced by ion-beam co-sputtering, RSC Adv. 5 (10) (2015) 7192–7195.
[50] N. Hornsveld, B. Put, W.M.M. Kessels, P.M. Vereecken, M. Creatore, Mass spectrometry study of Li_2CO_3 film growth by thermal and plasma-assisted atomic layer deposition, J. Phys. Chem. C 123 (7) (2019) 4109–4115.

[51] F. Li, Y.L. Liu, G.G. Wang, H.Y. Zhang, B. Zhang, G.Z. Li, Z.P. Wu, L.Y. Dang, J.C. Han, Few-layered Ti_3C_2T x MXenes coupled with Fe_2O_3 nanorod arrays grown on carbon cloth as anodes for flexible asymmetric supercapacitors, J. Mater. Chem. A 7 (39) (2019) 22631–22641.
[52] F. Han, J. Xu, J. Zhou, J. Tang, W. Tang, Oxygen vacancy-engineered Fe 2 O 3 nanoarrays as free-standing electrodes for flexible asymmetric supercapacitors, Nanoscale 11 (26) (2019) 12477–12483.
[53] P. Yu, M. Coll, R. Amade, I. Alshaikh, F. Pantoja-Suárez, E. Pascual, J.L. Andújar, E.B. Serra, Homogeneous Fe 2 O 3 coatings on carbon nanotube structures for supercapacitors, Dalton Trans. 49 (13) (2020) 4136–4145.
[54] H. Jiang, H. Ma, Y. Jin, L. Wang, F. Gao, Q. Lu, Hybrid α-Fe_2O_3@$Ni(OH)_2$ nanosheet composite for high-rate-performance supercapacitor electrode, Sci. Rep. 6 (1) (2016) 1–7.
[55] D.P. Dubal, W.B. Kim, C.D. Lokhande, Galvanostatically deposited Fe: MnO2 electrodes for supercapacitor application, J. Phys. Chem. Solids 73 (1) (2012) 18–24.
[56] P.M. Kulal, D.P. Dubal, C.D. Lokhande, V.J. Fulari, Chemical synthesis of Fe2O3 thin films for supercapacitor application, J. Alloy. Compd. 509 (5) (2011) 2567–2571.
[57] B.G. Sundara Raja, T.H. Ko, J. Acharya, M. –K. Seo, M. –S. Khil, H. –Y. Kim, B. –S. Kim, A novel Fe2O3-decorated N-doped CNT porous composites derived from tubular polypyrrole with excellent rate capability and cycle stability as advanced supercapacitor anode materials, Electrochim. Acta 334 (2020) 135627.
[58] Y. Wang, M. Zhang, D. Pan, Y. Li, T. Ma, J. Xie, Nitrogen/sulfur co-doped graphene networks uniformly coupled N-Fe2O3 nanoparticles achieving enhanced supercapacitor performance, Electrochim. Acta 266 (2018) 242–253.